Machine learning versus ETAS for earthquake forecasting in the Sea of Marmara: a leakage-audited negative result and a closed-form scoring artifact

Basri Kerem Alhan[1] (ORCID 0009-0007-8920-9239) and **Kenessary Khabat**[1] (ORCID 0009-0009-6830-7192)

[1] Sapienza University of Rome, Rome, Italy

Corresponding author: Basri Kerem Alhan (basrikerem@gmail.com), ORCID 0009-0007-8920-9239

This is a non-peer-reviewed preprint submitted to EarthArXiv.

Abstract

We ask whether machine learning adds 30-day earthquake-forecasting value beyond modern ETAS in the Sea of Marmara, a locked seismic gap beneath Istanbul, once leakage and scoring artifacts are controlled. On a homogenized KOERI catalog, feature causality is machine-checkable, and comparisons follow a pre-specified rule: paired block-bootstrap intervals on likelihood and ranking must agree. The ETAS×ML hybrid adds no ranking skill over a well-fit ETAS cascade. Its likelihood edge is inseparable from a scoring artifact with a closed form: count-scoring a clustered forecast against binary occurrence makes a(h) = h − 1 − ln h nats per positive recoverable by pure rescaling. Under a proper binary score, a small occurrence-recalibration edge survives, resolved in active cells and absent at M≥3.5; an ablation shows catalog features cannot reconstruct ETAS, and ranking information lives on the ETAS axis alone. The 2025 Mw 6.2 epicentral cell ranked in the top ~1–2% all year; the only escalation was a foreshock 36 minutes before rupture, and ~220 comparable alarms were followed by no M≥6.

Keywords: earthquake forecasting; ETAS; machine learning; data leakage; proper scoring rules; forecast evaluation; Sea of Marmara; foreshocks

Non-technical summary

The Sea of Marmara, located beneath the approximately 18-million-person Istanbul region, contains a locked fault segment that has not generated a large earthquake since 1766; a magnitude 6.2 event occurred in April 2025. This study investigates whether flexible machine learning methods enhance 30-day earthquake forecasts beyond the standard physics-based ETAS model, after controlling for two known sources of error: information leakage from the future into the model and scoring rules that may artificially favor one model over another. When leakage is made machine-checkable, and each evaluation is conducted on its appropriate terms, machine learning does not improve the ranking of hazardous locations. It provides only a modest improvement in the calibration of probability estimates, and a straightforward formula is presented to quantify the extent to which mismatched scoring conventions can generate apparent skill. The 2025 epicenter consistently ranked within the top 1–2% of cells throughout the year. However, the only advance indicator was a foreshock 36 minutes prior to the mainshock, which was indistinguishable from approximately 220 similar alarms that were not followed by a large earthquake.

1. Introduction

The Main Marmara Fault, the submarine continuation of the North Anatolian Fault beneath the Sea of Marmara, is the most prominent unbroken segment of a system that ruptured progressively westward across the twentieth century, culminating in the 1999 Mw 7.4 İzmit and Mw 7.2 Düzce events to its east. Its central portion has not produced a major earthquake since 1766 and lies directly offshore of Istanbul; long-term renewal calculations place the decade-scale probability of an M $\geq$ 7 beneath the sea in the tens of percent (Parsons, 2004). Nearly two decades of seismicity show an eastward progression of Mw > 5 events along the fault, described by the authors as a steady march toward the city (Martínez-Garzón et al., 2026); the 23 April 2025 Mw 6.2 (Mw 6.3 in some solutions) Kumburgaz earthquake, a strike-slip event at ~6 km depth on the central Marmara segment, is the most recent step in that sequence (Ertuncay et al., 2025). A mature seismic gap, a large exposed population, and an active migrating sequence make short-term forecasting here both consequential and demanding; they also make it essential that reported "skill" is not itself an evaluation artifact.

The operational standard for short-term forecasting is the Epidemic-Type Aftershock Sequence model (ETAS; Ogata, 1988): a background rate plus self-exciting Omori–Utsu aftershock cascades, underpinning the operational forecasting now run by national agencies (Hardebeck et al., 2024; Mizrahi et al., 2024). Neural point-process and deep-learning models have been proposed as a more flexible alternative (Dascher-Cousineau et al., 2023), but the head-to-head EarthquakeNPP benchmark found that neural models do not systematically beat a well-implemented ETAS under consistent, reproducible conditions (Stockman et al., 2026). A parallel review reaches the same conclusion from the methodological side: much of the exceptional skill reported in machine-learning earthquake forecasting reflects validation protocols that ignore the causal structure of seismicity, and it sets as a *minimum criterion* for practical utility that a candidate model demonstrably match or beat ETAS under strict, prospective, out-of-sample, likelihood-based evaluation (Jover-Alfaro et al., 2026). We meet that criterion directly, comparing against modern ETAS baselines (including an independent third-party inversion) under a pre-specified adjudication rule and catalog-based pyCSEP consistency tests.

Two artifact classes can inflate reported skill. The first is data leakage: information flowing from the evaluation target back into the features or the model selection. It is a leading driver of the reproducibility crisis in machine-learning-based science (Kapoor & Narayanan, 2023), and because rare large events are the quantity of interest, even a small target leak can manufacture apparent M6 skill that evaporates under forward validation; this is the failure mode behind a retracted Los Angeles prediction study (Yavas et al., 2024, retracted). We therefore make the absence of look-ahead *machine-checkable*: a truncated-catalog self-test recomputes every feature from a catalog truncated to the forecast time and requires it to reproduce the stored grid so that any reader can verify feature-level causality directly. The second class is subtler: a mismatch between the forecast quantity and the scoring rule. A gridded forecast has two distinct elicitable functionals, the expected event *count* in a cell-window and the *probability of at least one event* (occupancy), and a scoring rule elicited for one is improper for the other. Both conventions are in common use in machine-learning seismicity, and the distance between them turns out to be measurable in closed form.

This paper makes three contributions. (i) *An adjudicated negative result.* Under machine-checkable causality and a rule fixed before the final evaluation, an ETAS$\times$ML hybrid adds no ranking skill over modern, properly-fit ETAS baselines (a full recursive cascade Monte-Carlo forecaster, an EM-declustered variable-background variant, and the independent inversion), a finding that configuration variants only worsen (§4). This confirms the EarthquakeNPP finding under stricter causality control, on a fault where the answer carries direct societal weight. (ii) *A closed-form scoring-artifact identity.* The count-scored information gain of a clustered forecast, evaluated against a binary-occurrence target, carries a harvestable artifact $a(h) = h - 1 - \ln h$, recoverable in full by a pure rescaling that changes no ranking, with h the forecast's expected events per occupied cell-window. This quantity is exactly the Bregman divergence between the count and occupancy functionals (Brehmer et al., 2024); it is elementary within consistent-scoring theory, but to our knowledge unstated in the forecasting literature, and it is a property of the metric itself, independent of any model. (iii) *An ablation-based diagnosis.* Denied the ETAS channels, the gradient booster cannot reconstruct them from catalog features, and when it is handed every non-ETAS feature on top of ETAS its out-of-sample likelihood tends to worsen. The machine-learning stage, in short, recalibrates ETAS instead of finding new predictive structure. Two instruments bound these claims: a placebo battery that tests engineered channels against randomized, shifted and coverage-only surrogates of themselves, and machine-readable claims files that license every ranking stated here. Finally, we apply the same audited system to the 2025 Mw 6.2: an information-arrival analysis and a pre-registered false-alarm denominator separate the spatial question, which is tractable in rank, from the temporal one, which foreshock statistics bound. Throughout, we report probability *gain* relative to base rates and retain the negative results.

2. Data and study region

Region, grid and catalog. The model box spans 25.6–30.9° E and 39.6–41.9° N (Figure 1a), covering the Main Marmara Fault system and the northern strands of the North Anatolian Fault where the Kandilli Observatory and Earthquake Research Institute (KOERI) network is densest (Martínez-Garzón et al., 2026). Forecasts are made on a 0.1° grid (1,219 model-box cells) in 30-day windows: the ~8–11 km spacing balances fault-scale resolution against events per cell, and the 30-day window matches the horizon at which first-generation aftershock forecasting is reliable. For rare-event training only, a wide box (25.0–31.5° E, 39.0–42.5° N, 2,275 cells) captures more $M \geq 4.5$ events; models trained on it are always evaluated on the model box alone. The catalog is derived from the KOERI regional bulletin, 2003-01-04 to 2026-07-11 (frozen at fetch; the recent tail is preliminary and enters no metric), comprising 31,360 model-box events after deduplication. Three data-level issues were audited before any modeling (`docs/METHODS.md`): origin times were verified as true UTC against 21 independently recorded USGS/NEIC anchors ($M \geq 4.7$, residuals $\leq$ 3 s; `scripts/verify/tz_anchors.py`); 11,754 rows flagged in the source bulletin as suspected quarry blasts were screened out; and the untyped magnitude column was resolved as follows.

Magnitude homogenization and completeness (Figure 1b). The bulletin pools ML, Md, Mw and Ms without conversion, so magnitudes were typed and homogenized to a proxy-moment magnitude (`mag_w`) using the empirical relations of Kadirioğlu and Kartal (2016), applied (and flagged) slightly below their stated validity ranges for a small tail. Because the ML→Mw and Md→Mw offsets differ, this typing is what makes the completeness structure tractable and keeps all targets on one scale. Features, targets, and the primary ETAS fit use base Mc = 3.0: the modern M_L population completes near `mag_w` 2.72, so 3.0 is a conservative floor. The max-curvature completeness estimate, Mc = 3.65 (mode 3.45 + 0.2; Wiemer & Wyss, 2000), is inflated by ~15,000 Md events piling near `mag_w` 3.45 (Figure 1b); it reflects the Md conversion pile rather than the operative completeness of the modern, ML-picked population that dominates the 2022-onward test period. Mc is applied identically to feature counting, every baseline, and the common target labels, so residual sub-3.0 incompleteness is common-mode: it widens the paired bootstrap intervals (§3) but cannot manufacture a spurious between-model separation (Section S8). Because common-mode protection does not extend to the ETAS *fit* itself, we refit at Mc = 3.65 (dropping the incomplete Md era, an 86% reduction to 1,968 events): the triggering parameters are stable (productivity k -8%, α -3%, p +0.5%), the m_max-truncated branching ratio is unchanged (0.949 versus 0.950), and only the background normalization rescales, identically for every ETAS-derived forecaster (`results/catalog/mc_sensitivity.json`). Model-box counts are 5,024 events $\geq$ 3.5, 192 $\geq$ 4.5, 12 $\geq$ 5.5, and a single M $\geq$ 6 (the 2025 Mw 6.2; Table S3): every M6 number in this study therefore comes from Gutenberg–Richter extrapolation, synthetic validation, and wide-box checks, and no classifier is trained on the one positive. The mixed-magnitude character makes the b-value the dominant source of M6 extrapolation uncertainty (Mizrahi et al., 2021), so we carry a b ensemble (the Aki, 1965, maximum-likelihood b $\approx$ 1.02; b-positive $\approx$ 1.54, van der Elst, 2021; and an operational b_op = 1.15 adopted by convention, §3) and, above the conversion pile where the frequency–magnitude distribution is log-linear (M$\geq$4.0), a direct estimate b = 1.24 with a wide 95% interval [1.11, 1.40] (§3; Sections S10–S11).

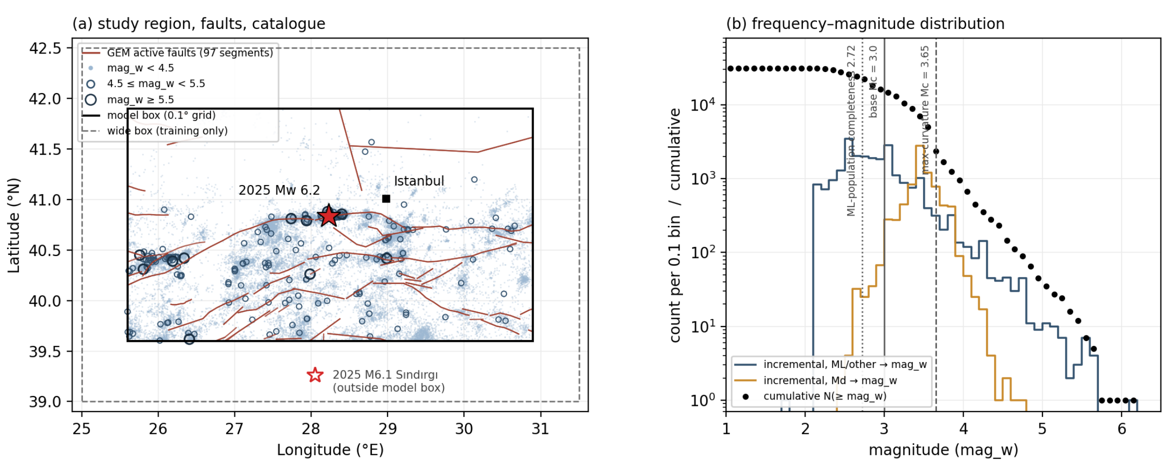

Figure 1: Study region and catalog. (a) Model box (solid) and wide training box (dashed), GEM active-fault traces, the homogenized model-box catalog, the 2025 Mw 6.2 Kumburgaz epicenter (filled star) and the out-of-box 2025 M6.1 Sındırgı event (open star). (b) Frequency–magnitude distribution of the 31,360 model-box events on the homogenized `mag_w` scale, split by source magnitude type. The Md-converted population piles near `mag_w` 3.45 and inflates the max-curvature completeness estimate (Mc = 3.65, dashed); the modern ML population completes near 2.72 (dotted), making the base Mc = 3.0 (solid) a conservative floor.

Fault model and stress inputs. The active-fault geometry is the GEM Global Active Faults Database (Styron & Pagani, 2020), reduced to 97 segments whose strikes orient anisotropic aftershock kernels and define Coulomb receiver planes. Time-causal Coulomb stress changes (ΔCFS) use an Okada (1992) half-space solution with King, Stein, and Lin (1994) resolution onto per-segment receivers; only ruptures preceding the forecast time contribute, with source parameters from published finite-fault models (Table S1). Interseismic strain is a static field from Nevada Geodetic Laboratory GNSS velocities (Blewitt et al., 2018), retained as a feature whose *marginal* predictive value is later tested and rejected (§4). The historical M~7 record (Ambraseys, 2002; Parsons, 2004) anchors a Brownian-Passage-Time renewal layer that is kept separate from the gridded products (Section S14).

3. Methods

Targets, functionals, and the model roster. Each 0.1° cell and 30-day window carries binary occupancy labels at three thresholds: M≥3.0 (the pre-specified primary target, 592 test positives), M≥3.5 (a powered secondary, 167), and M≥4.5 (unpowered, 22, diagnostic only; no ranking claims). Throughout, we separate the two elicitable functionals of §1, expected count and occupancy, and score each on its matched rule; the distance between the two conventions is quantified below. Table 1 lists the forecasters. Windows are split by start time into training (≤ 2021-12-31), validation (2022–2023), and test (2024-01-01 onward, target windows inside reviewed data, t0 + 30 d ≤ 2026-03-31); the split is strictly temporal, and all three ETAS variants estimate every triggering and background parameter on the training window alone. b_op is the sole quantity set on the wider pre-test span (through 2023), and no fit of any kind touches the test period.

Table 1. *The forecasters. The hybrid is the machine-learning challenger under test; the four physics forecasters and three reference baselines are what it must beat.*

Forecaster	Construction	Provenance
First-generation ETAS	analytic expected counts: background + first-generation offspring of the observed history	in-house maximum-likelihood fit
Cascade (ETAS-sim)	Monte-Carlo forward simulation: background + residual Omori + full recursive cascades, anisotropic kernels	same fit; simulator held subcritical
sv-ETAS	cascade with EM-declustered, spatially variable background (Zhuang et al., 2002)	in-house re-estimate
Independent inversion	third-party `etas` package fit (Mizrahi et al., 2024), integrated on our grid as a first-generation intensity	isolated environment; shares no code with ours
ETAS×ML hybrid	log-linear blend $\lambda_{\mathrm{sim}}^{1-w}\lambda_{\mathrm{ML}}^{w}$; Poisson gradient boosting on 19 causal features + ln λ_sim	the ML challenger
Reference baselines	Poisson climatology; smoothed seismicity; fault proximity	non-clustering floors

Features and the leakage self-test. Each cell-window carries 19 strictly causal features (Table S2): multi-scale event counts (30/90/365 d, in-cell and in 3- and 5-cell neighborhoods), times since the last M≥3.5 and M≥4.5 within 25 km, local b-positive, a short-/long-term rate ratio, mean depth, distance to the nearest fault, and the time-causal ΔCFS. The central safeguard is a truncated-catalog self-test: every feature is recomputed from a catalog truncated to < t0 and must reproduce the stored grid exactly, run exhaustively over every stored cell-window in train, validation and test: 258 windows (231 pre-test, one straddling the 2024-01-01 boundary that the b_op sweep excludes, and 26 test; the stored grid holds 4 further post-test windows, 262 in all) × 1,219 cells × 19 features = 5,975,538 checks, of which none fails, bit-for-bit with no tolerance. The largest absolute correlation between any feature and any target is 0.289 (`etas_rate` with the M≥3.0 label). Because every feature is causal by construction, truncation must be a no-op, which is what we observe. The test gates event-level look-ahead in the features; parameter-level leakage from fitting is a separate question (§6).

ETAS: fit, constraints, and validation. We fit a space–time ETAS by maximum likelihood (Ogata, 1988), with conditional intensity $\lambda(\mathbf{x},t) = \mu(\mathbf{x}) + \sum_{i:t_i<t} K\, e^{\alpha(m_i-m_c)}(t-t_i+c)^{-p} f(\mathbf{x}-\mathbf{x}_i;m_i)$, i.e. a background rate plus Omori–Utsu aftershock terms with a magnitude-dependent spatial

kernel; the background is estimated in the spirit of stochastic declustering (Zhuang et al., 2002). The implementation is validated in three independent ways. First, it passes 5/5 unit tests: recovery of known parameters from simulated catalogs (Veen & Schoenberg, 2008-style), a stable fit on the real catalog, causal filtering, Omori decay of the triggered rate, and Gutenberg–Richter consistency of the simulator. Second, an independent inversion of the same homogenized catalog with the third-party `etas` package (lmizrahi/etas; Mizrahi et al., 2024), run in an isolated environment with no shared code, provides an external comparator; we integrate its first-generation intensity on our grid to match our own first-generation baseline (a truncation on our side, not the package's; its CSEP number/magnitude rejections in §4 diagnose exactly that), with its native spatially variable background (a uniform-background floor is carried only as a pre-registered sensitivity; the one hybrid-versus-inversion separation that appears under the floor dissolves under the native background, marking it an integration artifact; Table S25). The package's b-positive estimate differs from ours (1.76 versus 1.54 on the identical catalog) only through estimator choice. Third, the simulation-based forecasters pass the catalog-based pyCSEP consistency tests (below). The branching ratio is capped subcritical at 0.95 under the fitting law (b = 1.54); the fit pins at this cap (raising it to 0.999 sends the estimate to the new cap), so the cap is an active stability constraint of the kind standard in operational ETAS practice, and §6 records its consequences. Because the operational cascade draws offspring magnitudes at b_op rather than the fitting b, holding the fitted productivity while shifting the magnitude law would raise the effective branching ratio to 1.21 (formally supercritical); we instead hold the realized branching ratio at 0.95 by rescaling the *simulated* productivity, $K_{\text{sim}} = n^*/n_1(b_{\text{op}})$ (equivalently K × 0.78, closed form in Section S1). Real-catalog parents keep the b-free maximum-likelihood productivity, so observed aftershock sequences are reproduced at full strength while the simulated cascade is subcritical by construction. A short-term aftershock-incompleteness correction (Helmstetter et al., 2006) is a null at base Mc = 3.0: it drops zero events, the post-M5.5 incompleteness window being sub-hour, consistent with the ETASI formulation of Hainzl et al. (2024). b_op = 1.15 is an operational convention, not a calibration: the pre-test count-calibration that produced it does not identify a magnitude law on this catalog (its objective reduces to the catalog's own counts, which the Md conversion pile contaminates; corrected, its optimum moves to 1.05 on the registered subsample and to 1.00 on all 231 pre-test windows), the above-pile law is only loosely identified (b = 1.24 [1.11, 1.40]), and every verdict in this paper is unchanged across b_op = 1.00–1.40 (Table S25; forensics in Section S10). The sv-ETAS variant re-estimates the background by expectation–maximization stochastic declustering; it turns out statistically indistinguishable from the first-generation model because the simpler background was already strongly spatially adaptive (coefficient of variation 1.27; Figure S1).

Cascade forecaster and hybrid. For each window, the cascade forward-simulates new background events, residual-Omori offspring of all prior history, and full recursive cascades (K = 500 simulations in backtests, 10,000 live), with offspring of M≥5.5 parents placed by an elliptical 3:1 kernel oriented along the parent's first 72 h aftershock principal axis or the nearest fault strike (Hardebeck et al., 2024; Mizrahi et al., 2024). Per-cell rare-magnitude rates are obtained analytically from the dense M≥3.5 rate field via Gutenberg–Richter. The forecaster passes a four-part gate: causality; reliability slope 0.949 on synthetic catalogs (within [0.8, 1.2]); a day-after-M6 rate 1.79× the first-generation expected counts (quantifying how first-generation ETAS under-counts active sequences); and along-strike anisotropy 2.77× (versus 1.06 isotropic). The hybrid, the machine-learning challenger, is the log-linear blend $\lambda = \lambda_{\text{sim}}^{1-w} \cdot \lambda_{\text{ML}}^{w}$, where λ_ML is a Poisson gradient-boosted regression on the 19 features plus ln λ_sim, and the single weight w is selected on the *validation* Poisson log-likelihood by a pre-registered one-standard-error rule (most cascade-leaning w within one bootstrap standard error of the maximum). The validation objective is not flat (it climbs ~216 nats from w = 0 to its optimum at the primary target), so the rule settles at w = 0.8 (argmax 0.9), and w = 0.4 (argmax 0.6) at M≥3.5. Monotonicity constraints tie both ETAS inputs and (negatively) fault distance, so the ML stage has structural access to both physics comparators as constrained inputs, and the blend's w = 0 endpoint recovers the cascade, so the challenger cannot lose to it by construction; it is the strongest challenger we could field under the causality constraints. Stripped of the cascade coupling, it loses to ETAS even with the first-generation rate retained (ΔIG

−0.605; Table S8, T1-7).

Registered scoring and adjudication. The registered metric is information gain (IG) in nats per positive relative to a baseline (the paired difference in total Poisson log-likelihood over all cell-windows, normalized by occupied cell-windows), through one shared scoring function (Rhoades et al., 2011), alongside precision–recall AUC (the ranking metric most sensitive to the rare positive class), ROC-AUC and the Brier score; Molchan/area-skill trajectories (Zechar & Jordan, 2008) are archived with every evaluation. Because IG and PR-AUC emphasize different things (likelihood mass versus rank ordering), a result is treated as robust only when the two agree: for each ordered pair and target we resample the 26 test windows with a stationary block bootstrap (Politis & Romano, 1994; mean block three windows, B = 2000, seed 42), keeping each window's 1,219 cells together; windows are temporally dependent through shared history, and a row-level bootstrap would understate variance (worst-case ~7× narrower intervals). A beats B only if both 95% intervals exclude zero in A's favor; otherwise the pair is *inseparable*. All 168 pairwise verdicts are emitted to a machine-readable claims file, and no ranking is stated in this paper that the file does not license. The rule is calibrated against a negative-control battery of twenty-eight same-model seed-pair refits: it flags none (0/28 under either scoring), every primary verdict is unchanged at mean block lengths 2, 3, 5 and 8, and a Benjamini–Hochberg sensitivity within five pre-specified families moves no registered separation (Section S11.4). The central comparisons are the hybrid-versus-physics pairs at the two powered targets; everything else is secondary or exploratory and adjudicates nothing. One disclosure governs all of this: models and hyperparameters were frozen before the final evaluation and tuned only on validation, but the claim rule and the primary endpoint were fixed *after* an exploratory pass had computed test-split metrics. The test set is therefore not pristine. Every later campaign was specified in a dated, hashed amendment before execution and re-scored frozen predictions rather than re-tuning anything; the full exposure history is tabulated in one place (Section S3, Table S8), and the hashed, append-only prospective log (below) is the forward remedy.

The count/occupancy identity and the proper score. Scoring an intensity forecast with a Poisson count likelihood against a binary occurrence label, a convention common in machine-learning seismicity, carries a quantifiable artifact for clustered forecasts: rescaling a forecast globally by s changes its mean per-positive log-likelihood by a closed-form amount maximized at $s^* = 1/h$, where $h = \Sigma\lambda/N_{\text{pos}}$ is the forecast's expected events per occupied cell-window, making $a(h) = h - 1 - \ln h$ nats per positive available from rescaling alone, a transformation that changes no ranking (derivation in Section S2). A count-calibrated clustered forecast therefore pays approximately a(m), with m the observed multiplicity, while an under-predicting forecast pays little. We therefore additionally score every forecaster with a proper binary score: the Bernoulli log-score on the model's own stated occurrence probability, the same occupancy target adopted in prospective CSEP proper-score evaluations (Bayona et al., 2022): native Monte-Carlo occupancy for the clustered simulators (K = 5000 catalogs, finite-K bias removed by 1/K extrapolation; Ferro, 2014), the exact $1 - e^{-\lambda}$ for first-generation intensities, and, for the hybrid, a bracket between two constructions on the cascade's catalogs (capped thinning versus thinning with independent top-up; we quote the conservative top-up value). A construction-free companion scores the analytic probability $1 - e^{-s_m\lambda}$ with one validation-fit scalar per model, isolating non-uniform recalibration. Four recalibration challengers, fit on pre-test data only, locate the ML stage within the space of recalibrations of the cascade: a single global scalar, a background/triggered pair $(s_{\text{bg}}, s_{\text{trig}})$, a static per-cell map, and an isotonic monotone map.

Consistency tests. We run the catalog-based CSEP consistency tests (number, magnitude, spatial and pseudo-likelihood; Savran et al., 2020) with the community pyCSEP toolkit (Savran et al., 2022), on 500 clustered catalogs emitted natively by each simulator over the test period. The independent inversion, integrated as a first-generation intensity, is Poisson-sampled at its own fitted b = 1.76, so its number/magnitude verdicts test that truncation, not the `etas` package. The hybrid's catalogs use the rate-exact top-up construction (mean total 1,041, matching $\Sigma\lambda$ = 1,040). An in-house Poisson rate cross-check reproduces every forecast mean to 0.1% but under-disperses the count distribution for clustered simulators and rejects where the native test accepts, the established reason Poisson consistency tests misfire for clustered forecasts (Kagan & Jackson, 2000; Werner et al., 2010); the native catalog-based run is therefore authoritative throughout.

Placebo battery for engineered channels. Because an engineered channel can enter the ML stage through spurious structure, a candidate channel must beat time-shuffled, circularly-shifted ($\geq$ 2 yr) and coverage-only surrogates of itself, each with full retraining, under a promotion rule fixed before the final evaluation (validation IG > +0.02 and test IG > 0). Two channels were tested: a GNSS deformation channel built from 22 continuous stations with strictly causal trajectory models (construction and EPOS cross-validation in Section S16), and a dense sub-Mc3 AFAD catalog.

The 2025 events: information arrival and the alarm denominator. To characterize *when* a target becomes forecastable, an information-arrival analysis freezes the system at strictly causal lead times (T−365 d to T−1 h, and just after any foreshock), recomputes all products from data available at each freeze, and tracks the target cell's spatial percentile and probability gain versus lead time (full analysis of three 2025 events in Section S13). Its complement is a pre-registered false-alarm denominator, with definitions fixed and hashed before the analysis ran: every mag_w $\geq$ 4.0 event in the model box is a qualifying trigger (n = 673 after a 365-day burn-in and a 30-day observability filter; 719 unfiltered), the alarm statistic is the identical countdown machinery evaluated at t + 10 min, and a hit is an M$\geq$6 within 30 days and 25 km (Section S5). A conditional large-event discriminator trained on renewal-timed synthetic ETAS sequences, a Foreshock Traffic-Light System overlay (Gulia & Wiemer, 2019), and a Brownian-Passage-Time renewal layer are carried as context layers (Section S14), and a monthly prospective job issues each 30-day forecast with a sha256 content hash written before the outcome is known, in an append-only log that cannot be revised in hindsight (Section S15).

4. Results

Benchmark verdicts (Table 2, Figure 2). At the primary target (M$\geq$3.0/30-day, 592 test positives) the physics forecasters cluster at the top (cascade PR-AUC 0.233, sv-ETAS 0.230, first-generation 0.223, independent inversion 0.206) and the ETAS$\times$ML hybrid sits with them (0.226). Under the registered rule, the hybrid is inseparable from all four physics models: it gains likelihood over the clustered simulators (hybrid versus cascade +0.29 nats [+0.20, +0.43]) while trailing first-generation ETAS on that axis, its PR-AUC differences are not significant, and it beats the non-clustering baselines (versus smoothed +0.10 PR-AUC [+0.08, +0.13]). That likelihood edge is carried entirely by the total-rate term of the decomposition, the signature of a recalibration; we develop this below. Within the physics cluster, cascade, sv-ETAS and first-generation ETAS are mutually inseparable; first-generation ETAS separably beats the independent inversion under matched inputs (information gain +0.28 [+0.05, +0.50], ΔPR-AUC +0.017 [+0.005, +0.029]), a secondary separation that proper scoring localizes to ranking (below). At M≥3.5 (167 positives) the picture repeats: the hybrid is inseparable from the physics cluster, every ETAS variant beats Poisson climatology (cascade +0.96 nats [+0.48, +1.52]), and the value the cascade adds is concentrated *inside active sequences*, where it produces ~1.8× more offspring than first-generation ETAS. All of this is stable in the operational magnitude law: re-running the entire pipeline at b_op = 1.10, 1.15 and 1.20, and at the contested endpoints 1.00 and 1.40, leaves every hybrid-versus-physics verdict inseparable and every physics-versus-physics verdict unchanged (Table S25, Section S10.5). A post-review sensitivity replacing the ML stage's internal early-stopping split with a grouped-temporal rule moves no anchoring verdict, but first-generation ETAS then separably beats the hybrid at both targets: the reported inseparability is therefore a ceiling on the ML stage's standing, not a floor (Section S9). The M≥4.5 target (22 positives) supports no ranking claim and is retained as a diagnostic: the model-box hybrid takes the highest PR-AUC (0.076 versus the cascade's 0.062) while being miscalibrated (Brier 0.00102 versus 0.00068; information gain −3.76 nats per positive against the cascade), a pathology the identity below decomposes; the production M≥4.5 product is the cascade's analytic Gutenberg–Richter rare-rate field (Section S15).

Table 2. *Test-set benchmark at the operational b_op = 1.15, both powered targets. The physics models are inseparable among themselves except that first-generation ETAS beats the independent inversion; the hybrid is inseparable from all of them at the registered configuration and beats the non-clustering baselines; verdicts are unchanged across b_op = 1.00–1.40 (Table S25).*

Predictor	M≥3.0: PR-AUC	ROC-AUC	Brier	M≥3.5: PR-AUC	ROC-AUC	Brier
Cascade (ETAS-sim)	**0.233**	0.876	0.0168	**0.131**	0.880	0.00495
sv-ETAS	0.230	0.876	0.0168	**0.131**	0.877	0.00496
Hybrid (cascade × ML)	0.226	**0.881**	0.0166	0.130	0.884	**0.00492**
First-generation ETAS	0.223	0.880	**0.0164**	0.126	0.894	0.00497
Independent ETAS fit (first-gen integration)	0.206	**0.881**	0.0167	0.111	**0.897**	0.00502
Smoothed seismicity	0.125	0.869	0.0192	0.044	0.886	0.00544
Poisson climatology	0.124	0.856	0.0176	0.032	0.848	0.00532

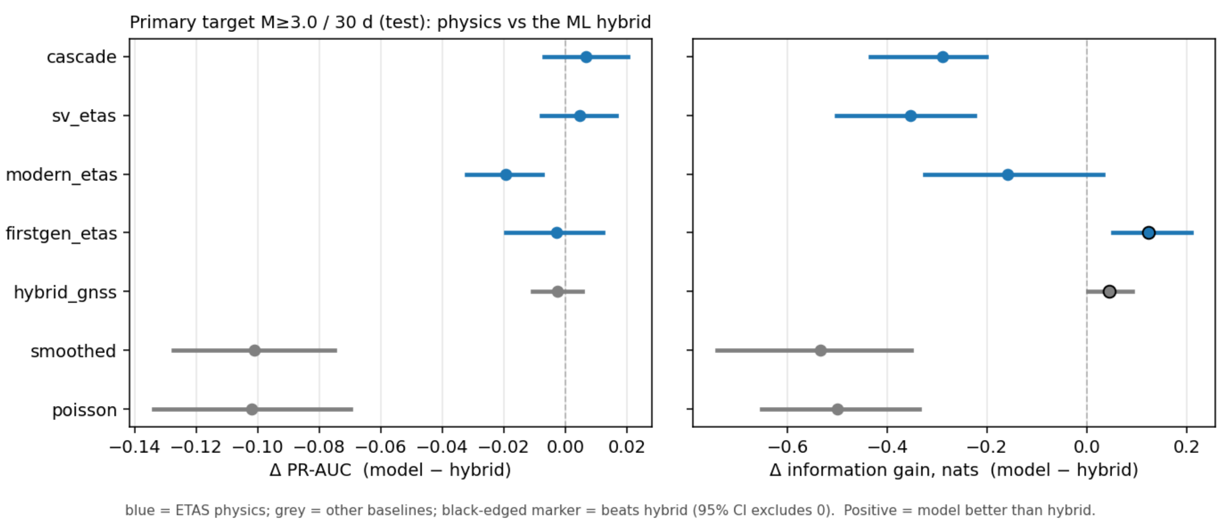

Figure 2: Primary target (M≥3.0/30-day, test set): paired differences (model − hybrid) in PR-AUC (left) and information gain (right) with 95% stationary-block-bootstrap confidence intervals, at the operational b_op = 1.15. Under the conjunctive rule each physics model is inseparable from the hybrid: at least one of its two paired-difference intervals straddles zero, so the requirement that both exclude zero is unmet (for the clustering models the PR-AUC interval straddles, for the inversion the information-gain interval does); this holds across b_op = 1.10, 1.15 and 1.20 (Table S25).

The scoring artifact, realized (Figure 3). The hybrid's registered likelihood edge over the cascade (+0.29 [+0.20, +0.43]) splits, through the identical scoring code, into a total-rate term of +0.450 and a *negative* ranking-mass placement term of −0.161 nats per positive: the ML trims the cascade's over-prediction of the quiet background; it does not move mass toward the events. The identity of §3 quantifies how much of such an edge scoring geometry alone supplies: on the test windows the cascade's h is 2.206, making a(h) = 0.415 nats per positive available from a rescaling that changes no ranking. A single validation-fit scalar (s = 0.423, against the test-optimal 0.453) realizes it to within 0.003 (measured +0.412 [+0.32, +0.52] against the cascade, exactly the identity's prediction at that s) and is statistically inseparable from the hybrid (paired ΔIG +0.124 [−0.02, +0.25]; ΔPR-AUC +0.007 [−0.007, +0.020], identically the cascade–hybrid ranking difference, as a monotone rescale must be). The hybrid's registered edge therefore sits entirely within the calibration headroom the identity makes available: on the registered axis the ML stage is indistinguishable from one constant. The identity also makes a quantitative prediction: scored at each forecaster's own optimum, the count-to-occurrence shift equals a(h_A) − a(h_B) exactly. The empirical content is whether the pipeline's validation-fit scalars realize it, and among the calibrated forecasters they do, to within 0.01 nats (worst case 0.0074). Across targets the cascade's h falls 2.206 → 2.085 → 1.122 (M≥3.0/3.5/4.5) and the artifact vanishes along the curve, 0.415 → 0.350 → 0.007 (Figure 3); the one outlier is the overfit model-box M≥4.5 hybrid (h = 4.98), whose −3.76-nat deficit decomposes into ≈2.4 nats of calibration geometry, a(4.98) − a(1.122), plus ≈1.4 nats of genuine misallocation.

Proper-score re-adjudication (Table 3). Re-scored on the matched occurrence functional, the picture inverts: the artifact is gone, and a smaller, real edge resolves that the registered axis was too artifact-dominated to see. The hybrid's surviving edge over the cascade is +0.095 [+0.051, +0.147] nats per positive under the conservative construction (bounded above by +0.183; construction-free proxy +0.099), robust across the whole contested magnitude-law range (+0.110, +0.107, +0.102 at b_op = 1.00, 1.15, 1.40, everywhere excluding zero; arm machinery at K = 2000, undebiased, hence the small offset from +0.095; Section S10.5), with a finite-simulation debias that is linear in 1/K ($r^2 = 0.99$). Re-scoring every registered pair under this secondary proper score changes no verdict of record, and the two-axis verdict remains inseparable: on the ranking axis the pair is unresolved (intensity ΔPR-AUC −0.007 [−0.020, +0.007]), and occupancy-based ranking is construction-dependent (+0.009 capped, −0.015 top-up). The challengers locate the

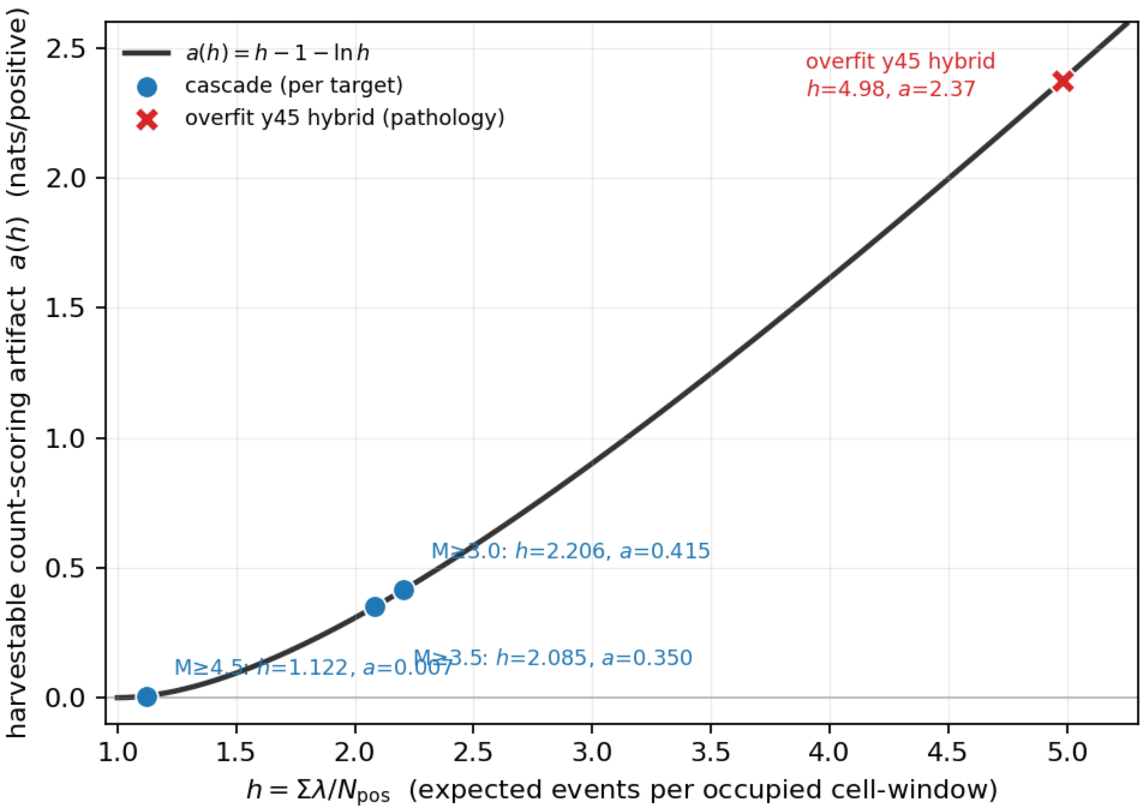

Figure 3: The count-scoring identity. The curve is the artifact $a(h) = h - 1 - \ln h$ (nats per positive) available from a pure rescaling that changes no ranking, against $h = \Sigma\lambda/N_{\mathrm{pos}}$, the forecast's expected events per occupied cell-window. Each forecaster is placed at its measured h; the cascade traces the curve across targets (M≥3.0/3.5/4.5: h = 2.206 → 2.085 → 1.122, a = 0.415 → 0.350 → 0.007 as $h \to 1$). The overfit model-box M≥4.5 hybrid ($h = 4.98$) is the labeled outlier (the pathology of §4) rather than a counterexample.

residual. A static per-cell map reproduces none of it (+0.004 [−0.043, +0.052]): the edge is dynamic. Two physics constants recover about half (background/triggered rescale s_bg = 0.46, s_trig = 0.40, gaining +0.046 [−0.005, +0.142]), while the hybrid retains a resolved dynamic remainder of +0.053 [+0.018, +0.085]. By regime, the edge is resolved where sequences are running (recently active cells +0.079 [+0.040, +0.124] over 280 positives, resolved in both pre- and post-Kumburgaz windows), unresolved in quiet cells (+0.117 [−0.004, +0.325]), intact under leave-Kumburgaz-out (Section S11.3), and absent at M≥3.5 (−0.035 [−0.090, +0.028]), where the smaller h left less calibration headroom; this outcome was predicted in the hashed amendment before the run. Among the physics forecasters, the proper score changes no two-axis verdict. The cascade carries a single-axis occurrence deficit against first-generation ETAS (−0.056 [−0.097, −0.032]): clustering costs occurrence calibration and buys back only ranking. The raw occupancy totals show the geometry directly (cascade 1.53×, sv-ETAS 1.51×, hybrid 1.26×, first-generation 1.15×, inversion 0.88× the 592 realized positives; Table S26). The cascade's over-forecast is the occupancy face of its spatial-test failure: it simulates 1.44 events per occupied cell-window where the catalog delivers 2.34, a 1.62× within-cell multiplicity deficit. The independent inversion is the best occurrence-calibrated forecaster in the study and no likelihood separation from it survives the proper score; what survives on the ranking axis is uniform (cascade over inversion ΔPR-AUC +0.026 [+0.010, +0.041] at every operational b), so the apparent non-transitivity of the registered verdicts resolves into a likelihood-axis handicap differential and is not a property of the models themselves. Under every scoring, the same conclusions hold (Table 3): the ML stage adds no ranking skill; the cascade and first-generation models out-rank the truncated inversion; and the stage's real contribution is a small, dynamic, active-cell occurrence recalibration whose registered-score magnitude was statistically indistinguishable from calibration geometry with a closed form.

Table 3. *Primary target (M≥3.0/30-day, test), headline pairs under three scorings, all ΔIG in nats per positive, reported as (A − B). Registered = count-scored adjudicator of record; Bernoulli-native = proper binary log-score on native Monte-Carlo occupancy, conservative (top-up) construction, points debiased by 1/K extrapolation with intervals at the operating K = 5000 (sole*

exception cascade vs sv-ETAS, raw K = 5000; see †); Proxy = construction-free Bernoulli on the per-model-scalar occurrence probability. Ranking (ΔPR-AUC) is score-invariant.

Pair (A vs B)	Registered ΔIG	ΔPR-AUC	Verdict	Bernoulli-native ΔIG	Proxy ΔIG
hybrid vs cascade	+0.29 [+0.20, +0.43]	−0.007 [−0.020, +0.007]	inseparable	+0.095 [+0.051, +0.147]	+0.099 [+0.034, +0.199]
cascade vs first-gen	−0.41 [−0.56, −0.30]	+0.010 [−0.005, +0.027]	inseparable	−0.056 [−0.097, −0.032]	−0.014 [−0.112, +0.057]
cascade vs inversion	−0.13 [−0.42, +0.09]	+0.026 [+0.010, +0.041]	inseparable	+0.017 [−0.108, +0.139]	+0.051 [−0.113, +0.198]
first-gen vs inversion	+0.28 [+0.05, +0.50]	+0.017 [+0.005, +0.029]	separable (secondary)	+0.073 [−0.043, +0.199]	+0.065 [−0.041, +0.187]
cascade vs sv-ETAS	+0.065 [−0.033, +0.192]	+0.002 [−0.005, +0.009]	inseparable	−0.011 [−0.017, −0.006]†	+0.068 [−0.029, +0.190]

†Raw K = 5000, not debiased, and to be read as ≈ 0: the two simulators share a per-window seed, so their Jensen biases largely cancel and no 1/K trend survives to be removed. The pair stays inseparable regardless: the ranking axis straddles zero, so the conjunctive rule is unmet whatever the likelihood axis does.

Ablation: what the features actually carry (Table 4). A feature ablation and grouped principal-component study (run post-review; full design and tables in Section S12) turns the recalibration reading into a causal statement. Pure Poisson-boosted *rate* models (no cascade blend, so each score measures its feature set's information content) are fit on nested feature subsets under the identical splits, scoring and bootstrap. This yields three findings. First, the catalog features do not reconstruct the ETAS intensity: denied the two ETAS channels, the booster loses to the ETAS-features-only model (−0.41 [−0.79, −0.21]) and to the raw cascade (−0.31 [−0.70, −0.07]); ETAS is a compact sufficient statistic of the catalog at this data scale. Second, flexibility itself costs: giving the booster all 18 non-ETAS features on top of ETAS *worsens* out-of-sample likelihood (−0.21 [−0.42, +0.01]; per-window sign 10+/16−), which makes the effective-sample-size concern concrete. Third, the one stable addition is static geophysics (ΔCFS, strain rate, fault distance): +0.22 [+0.15, +0.30] likelihood, but a ranking gain of only +0.006 (two-axis inseparable) and a calibration that does not surpass the analytic first-generation ETAS itself (Bernoulli LL/positive −3.83 versus

−3.80), so its contribution is rate recalibration toward a hazard geography that a better-calibrated ETAS already encodes. The two ETAS generations carry non-redundant information (jointly +0.044 [+0.020, +0.069] over cascade-features-only), and the ETAS-features-only booster's own edge over the raw cascade (+0.105 [+0.000, +0.223], ranking −0.013) reproduces the paper's likelihood-not-ranking layer as an ablation. Grouped PCA puts the 20 inputs at ~15 linear but only ~6 predictive axes, and grouped permutation under the full model concentrates the ranking information on the ETAS axis alone: permuting the ETAS block costs 0.149 of PR-AUC; every other block costs ≤ 0.031.

Table 4. *The ablation ladder at the primary target (M≥3.0/test, 592 positives). ΔIG is the count-convention Poisson information gain per positive against the ETAS-features-only booster, stationary block bootstrap [95% CI]; the analytic first-generation row enters as a calibration reference only and carries no ΔIG entry; full study in Section S12.*

feature set (n features)	PR-AUC	Bernoulli LL/pos	ΔIG vs ETAS-only [95% CI]
cascade (raw rate, reference)	0.233	−4.12	−0.105 [−0.223, −0.000]
first-generation ETAS (analytic, reference)	0.223	−3.80	—
ETAS features only (2)	0.219	−4.03	0 (reference)
ETAS + static geophysics (6)	0.225	−3.83	+0.22 [+0.15, +0.30]
ETAS + recent counts (10)	0.200	−4.09	−15.2†
full (20)	0.173	−4.14	−0.21 [−0.42, +0.01]
recent counts only (8)	0.194	−4.03	−0.07 [−0.20, +0.07]
catalog, no ETAS (14)	0.144	−4.40	−0.41 [−0.79, −0.21]
catalog + geophysics, no ETAS (18)	0.156	−4.30	−0.32 [−0.59, −0.11]

† A count-space pathology, not a ranking one: this variant assigns $\Sigma\lambda$ = 10,217 expected test events against 1,383 observed while its Bernoulli and ranking scores stay ordinary; raw multiscale counts let a Poisson booster extrapolate the rate scale on unseen feature combinations, which the shipped hybrid's geometric blend caps structurally. Its heavy-tailed per-window deltas destabilize the bootstrap CI for this one pair, which is why no CI is quoted.

CSEP consistency and the ranking–calibration gap (Figure 4). Over the test period (1,383 observed M≥3.0 events) the catalog-based tests separate the count from its spatial distribution. The cascade is count-consistent (forecast mean 1,306; number-test quantile 0.094) and magnitude-consistent (quantile 0.25), as is sv-ETAS (1,296; 0.080); the pass rests on the clustered count dispersion, and an analytic-Poisson number test would spuriously reject here. The independent inversion, integrated as a first-generation intensity, under-predicts by 43.4% (782 versus 1,383) and fails the number and magnitude tests, as any first-generation intensity without secondary triggering must; the rejection diagnoses our truncation, not the `etas` package. The cascade and sv-ETAS fail the spatial and pseudo-likelihood tests on their own native clustered catalogs: a real spatial mis-allocation, with rate spread too smoothly (over-weighting the quiet background and under-weighting the Kumburgaz aftershock zone) that persists after renormalizing the zone and background totals, so the defect is finer-grained than a two-region imbalance. The hybrid sharpens this trade-off into an incompatibility: its catalogs average 1,041 events, the very rate-trim that earns its occurrence likelihood, so the number test rejects it (1,041 versus 1,383) where it accepts the cascade, while it stays magnitude-consistent (quantile 0.61) and fails the spatial tests exactly as the cascade does. A single rate field cannot be both count-calibrated and occurrence-calibrated under clustering; the registered count rule and the occurrence proper score pull the same forecaster in opposite directions, which is why neither axis alone adjudicates the ML stage.

Engineered channels: placebo-controlled nulls (Figure 5). Neither engineered channel was promoted. On the operational M≥3.0 target, the GNSS-augmented hybrid showed a small likelihood gain (+0.045 [+0.001, +0.091] nats per positive) and no ranking gain (ΔPR-AUC −0.003 [−0.011, +0.005]); at M≥3.5 it was actively worse (−0.053 [−0.088, −0.022]). The two temporal surrogates fail to void the likelihood gain (time-shuffle null band [−0.151, +0.036]; circular shift [−0.059, +0.039]); the coverage-only surrogate voids it: a single count of GNSS stations reporting within 60 km (station availability, carrying no deformation whatever) recovers +0.043 of the +0.045, i.e. 96% of the effect, and 30% of it falls in a single window. The channel's apparent gain is a spatial-availability proxy, and we report GNSS as a null that supersedes the earlier static-strain null

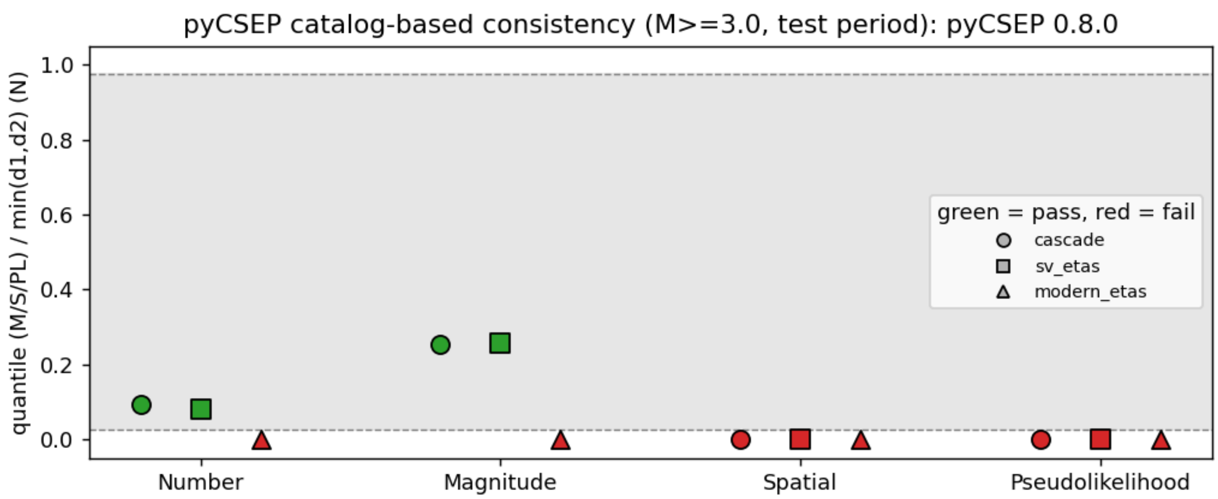

Figure 4: pyCSEP catalog-based consistency tests (M≥3.0, test period) at the operational b_op = 1.15, computed from each model's own simulated clustered catalogs: quantiles of the number, magnitude, spatial and pseudo-likelihood tests (green = consistent at α = 0.05, red = rejected). The cascade and sv-ETAS are count- and magnitude-consistent but fail the spatial and pseudo-likelihood tests, a spatial mis-allocation of the correct total rate; the independent inversion (integrated as a first-generation intensity) under-counts and fails the number and magnitude tests, a consequence of that first-generation truncation on our side, not of the `etas` package. The ML hybrid is not shown; its test outcomes are given in the text (the number test rejects it, 1,041 versus 1,383, but accepts the cascade).

with a stronger, feature-engineering-robust one. The dense sub-Mc3 catalog likewise failed the gate: test information gain positive and interval-significant (+0.130 [0.045, 0.229]) but *validation* gain negative (−0.030), a sign disagreement consistent with completeness non-stationarity (Section S16). Statistical significance was necessary but not sufficient in either case; the placebo battery adjudicated the GNSS channel, and the pre-specified validation gate adjudicated the dense catalog.

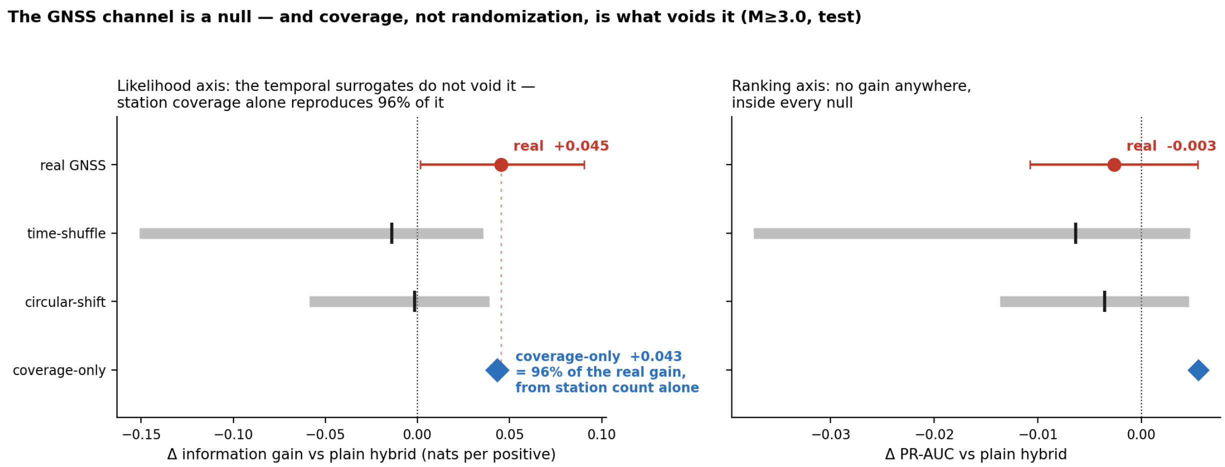

Figure 5: The GNSS channel is a null, and the coverage surrogate is what voids it. Left: on the operational M≥3.0 target the real Δ(information gain) from adding GNSS (+0.045, red) marginally clears the time-shuffle ([−0.151, +0.036]) and circular-shift ([−0.059, +0.039]) null bands, so the two temporal surrogates do not void the channel. The coverage-only surrogate does: a single count of GNSS stations reporting within 60 km, carrying no deformation, reproduces +0.043 of the +0.045. Right: the ranking axis shows no gain at any point (ΔPR-AUC −0.003 [−0.011, +0.005]), inside every null. A battery of temporal surrogates alone would have promoted this channel.

The 2025 Mw 6.2: spatial rank, temporal boundary (Figure 6). The same audited system, read against the April 2025 mainshock, returns a where-versus-when decomposition. Spatially, the epicentral cell was the 99.3rd-percentile cell by P(M≥6) at a strictly causal freeze the day before the mainshock (a 4.74× gain over a uniform baseline), and its percentile stayed flat at ~98–99 all year (Figures S2–S3). This is a statement about relative ranking, not absolute spatial calibration: the same forecasts fail the CSEP spatial tests above. Temporally, the cell was quiescent throughout (0–2 M≥2 events per 30 d) and the 30-day M≥6 probability gain held at ~4–7× until the lone M_L 4.0 (proxy-Mw 4.5) foreshock, 36 minutes before rupture: ten minutes after it the cell jumped to the 99.9th percentile and the gain rose to 39.7× (30-day P(M≥6) from 0.009% to

0.076%). The pre-registered denominator puts that escalation in context. Escalation after an M≥4 trigger is routine: every one of the 673 qualifying triggers in the catalog raised its cell's 30-day P(M≥6) by at least 5.6×, and the median trigger raised it 24.5×. At the ≥10× threshold, 621 of 673 triggers (92.3%) escalate, exactly one was followed by an M≥6, and the false-alarm ratio is 99.84% (precision 1 in 621). The Kumburgaz foreshock's 39.7× sits at the 67th percentile of that distribution: 219 other triggers matched or exceeded it, and none was followed by an M≥6 (Figure 6). Absolute probabilities stay small throughout: after the foreshock, about one in 1,300, and the most alarming trigger in 23 years reached 1.78%, about one in 56. The alarms persist rather than decay (37.5% of ≥10× escalations remain above threshold at +30 d; Table S10b). At the ≥40× sensitivity threshold there are 217 escalations, zero hits, and an exact 95% (Clopper–Pearson) upper bound on precision of 1.7% (full accounting in Tables S10–S10c). The foreshock therefore carried information: the escalation is real, causal, and the largest update in the event's own information-arrival curve. But an escalation of that size is the routine consequence of any M≥4 here; it marks elevated hazard and could not have functioned as a warning. A decision rule acting on it would have acted 621 times in 23 years for one success. The conditional discriminator and FTLS layers do not change this reading: on the two real 2025 sequences the synthetic discriminator does not separate sequence-preceded from cold-start escalation, and the surviving contrast (the FTLS reaches red for the developed Sındırgı sequence but never classifies the cold-start Kumburgaz one) is illustrative on n = 2 and not a calibrated skill estimate (Sections S13–S14). The live operational products, their pseudo-prospective calibration battery (every product calibrated in the mean; obs/exp 1.02 at M≥3.5), and the b-ensemble probability bands they are issued under are given in Section S15 and Tables S4–S5.

5. Discussion

The central negative result is stable. The EarthquakeNPP benchmark found that flexible models do not beat a well-implemented ETAS (Stockman et al., 2026); our benchmark reaches the same conclusion under stricter causality control, on a single fault where the answer matters. The physics

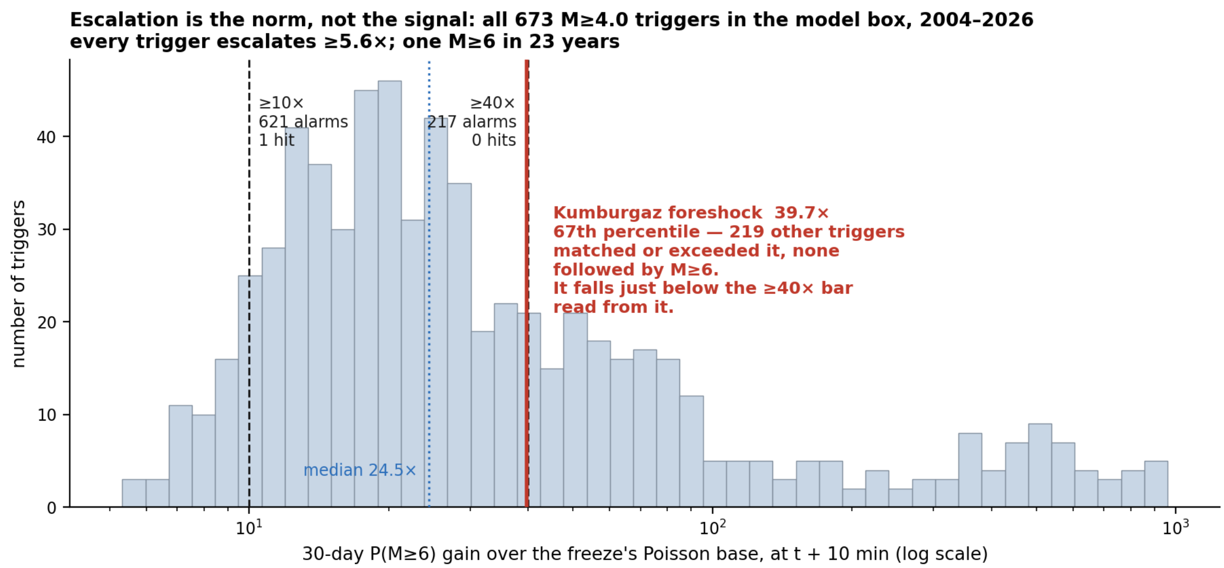

Figure 6: The foreshock escalation in context: distribution of the 30-day P(M≥6) gain at t + 10 min over all 673 qualifying M≥4.0 triggers in the model box (2004–2026), on a log axis. Every trigger escalates by at least 5.6×; the median escalates 24.5×. The Kumburgaz foreshock (red) escalated 39.7×, the 67th percentile, and is the only trigger in the catalog followed by an M≥6 within 30 days and 25 km. The ≥10× and ≥40× thresholds are marked: 621 and 217 triggers cross them, with one and zero hits respectively.

forecasters are stable and largely inseparable, their verdicts unmoved by the operational magnitude law, and the hybrid shares that stability: inseparable from every physics forecaster at the registered configuration, inseparable across the b_op range, superior under no examined configuration, with several reasonable training variants worsening its ranking (§4, Section S9). The negative result survived every attempt we made to break it, including leave-Kumburgaz-out (Section S11.3), multiplicity adjustment (Section S11.4), and re-selection of the blend weight under the proper score itself, which moves w only from 0.8 to 0.6 (round-3 archive).

What the ML stage does do is now characterized in three layers that disagree with one another. Under the registered count-scored rule, it holds a likelihood edge that a single validation-fit constant matches; on that axis the ML stage cannot be distinguished from one number. Under the proper occurrence score, the artifact is gone and a smaller, real edge resolves: dynamic (no static per-cell map reproduces it), resolved in active cells, about half recoverable by two refitted ETAS calibration constants, and absent at M≥3.5. On ranking the stage adds nothing under any measure examined. The ablation gives this reading its causal form: the booster cannot reconstruct ETAS from the catalog features, extra flexibility tends to hurt out-of-sample likelihood, the one stable feature addition is likelihood-only, and the ranking information is confined to the ETAS axis. Of ~20 engineered inputs, there are ~15 linearly independent axes, ~6 predictively independent ones, and one ranking axis, the ETAS intensity.

The mechanism is a measured one. Occurrence-optimal trimming discounts the triggered component harder than the background (s_trig = 0.40 < s_bg = 0.46) because triggered events stack within cells and occupancy saturates: the cascade simulates 1.44 events per occupied cell-window where the catalog delivers 2.34, a 1.62$\times$ within-cell multiplicity deficit that underlies its spatial-test failure, its 1.53$\times$ occurrence over-forecast, and the scoring artifact alike. The artifact's decline with threshold (0.415 $\rightarrow$ 0.350 $\rightarrow$ 0.007) is a measured instance of earthquake-number over-dispersion falling toward Poisson as magnitude rises (Kagan, 2010). The same defect appears in both a temporal and a spatial split: the cascade over-predicts the quiet pre-Kumburgaz interval by 1.47$\times$ and under-predicts the active post-mainshock interval (0.65$\times$); over-weights the diffuse background by 1.40$\times$ and under-weights the aftershock zone (0.49$\times$). Refitting the branching cap at 0.95, 0.98 and 0.99 leaves the splits unchanged, so this is a productivity ceiling, not a cap artifact: the signature of a single stationary productivity failing to hold the rate variance of a non-stationary sequence. The same reading tempers the steady-march interpretation of the migration (Martínez-Garzón et al., 2026). The refinement these results point to is physical rather than statistical: a spatially varying productivity K($\mathbf{x}$) and a time-varying background $\mu(\mathbf{x}, t)$ would live exactly where the ML stage's surviving contribution lives. Where our cascade does add value (inside active sequences, and in the analytic rare-rate field) the value comes from the physics of the simulation, not from the regressor.

Some methodological lessons carry beyond this study. First, on a sufficiently clustered catalog an improper scoring convention can supply more apparent skill than the real differences between forecasters: the artifact capacity here (a $\approx$ 0.415 nats per positive at h $\approx$ 2.2) exceeds the largest genuine inter-model edge in the study ($\approx$ 0.10) by roughly a factor of four. Count-scoring binary occupancy is common in machine-learning seismicity; proper binary alternatives are established (Serafini et al., 2022; Zechar & Zhuang, 2014), full point-process likelihoods of the EarthquakeNPP kind are unaffected (Stockman et al., 2026), and the community's three current fixes (occurrence recalibration, proper binary scoring, multiplicity adjustment) address the same within-cell clustering from three sides (Mizrahi et al., 2024). Second, block-bootstrap significance can certify structured noise: both engineered channels cleared the conventional interval bar, and only the placebo battery, specifically a coverage-only surrogate that temporal randomization cannot substitute for, exposed the GNSS gain as a station-availability proxy. Third, a calibration objective can return a precise, reproducible number that measures the data's artifact structure rather than the intended quantity: the operational-b count-calibration reproduces to seed variability sd ≈ 0.002 yet moves a full grid step with the era, threshold or window subset, because it reads the catalog's conversion mixture instead of a magnitude law (§3, Section S10). Leakage, the scoring rule, and the calibration objective share a failure mode: each returns a precise, defensible number that is an artifact of the structure of the data. In each case the defense that worked was a surrogate, a proper score, or a reported span; a tighter interval would not have helped.

The 2025 Mw 6.2 fixes the operational reading. The spatial problem is tractable in a specific and limited sense: the model discriminates (the epicentral cell sat in the top ~1–2% of cells for a full year) while remaining spatially mis-calibrated in absolute terms, so the product is useful for prioritization but not yet as a probability map. The temporal problem is different in kind: the only event-specific information arrived 36 minutes before rupture, and the denominator shows an escalation of that size to be the routine consequence of any $M \geq 4$ in this catalog, consistent with long-standing arguments that the timing of large events is intrinsically hard to forecast (Geller et al., 1997; Vere-Jones, 1998). The appropriate posture is a standing, well-calibrated spatial hazard map that is transparent about its temporal limits, plus a sequence-triggered alert layer whose false-alarm and miss characteristics are stated up front (Jordan et al., 2011), with cold-start mainshocks, of which the Mw 6.2 was effectively one, explicitly outside its reach. On communication: we issue probability *gain* relative to base rates, and the gain is the least robust number we publish: against the b-free base rate the 30-day $M \geq 6$ product ranges from $10.7\times$ at b = 1.02 down to $0.37\times$ at b = 1.54, and at the count-anchored end of the above-pile interval ($b = 1.40$) it sits at $0.86\times$, i.e. essentially at the base rate. What we stand behind is the ensemble range (Section S15), which bounds the hazard to within an order of magnitude, is consistent with the established long-term picture (Parsons, 2004), and nowhere exceeds it. Nothing in these results implies an imminent large earthquake.

What transfers beyond Marmara is chiefly the protocol: causality made machine-checkable; comparisons adjudicated on likelihood and ranking under a rule fixed before evaluation; each question scored on its matched functional, with the count/occupancy divergence reported in closed form; engineered channels gated against coverage-only as well as randomized surrogates; and prospective credibility accrued through a hashed, append-only log. Applied elsewhere, the same protocol catches the two artifact classes that inflate reported skill, leakage and functional mismatch; Table S27 tabulates the findings by evidentiary tier and portability.

6. Limitations and future work

The binding limitation is the effective information content of the test set: though the primary target carries 592 positives, the temporal inferential unit is 26 windows, so every interval rests on a small number of temporal blocks and single sequences can dominate windows. The study covers one region with a single real M6: the large-event statements rest on Gutenberg–Richter extrapolation and synthetic validation, the $M \geq 4.5$ target is unpowered, and the negative ML result is best read as a single-region confirmation, under stricter leakage control, of the multi-region EarthquakeNPP finding. The audit machinery is region-agnostic, and the open gates are a direct invitation to replicate elsewhere. The test set is not pristine: it was scored in four evaluation campaigns, each later campaign specified in a dated, hashed amendment before execution, with the full exposure history in Section S3; the binary-occurrence proper score was specified after the registered adjudication and is reported alongside it, never in place of it. The causality self-test covers event-level look-ahead in features only; it does not extend to parameter-level leakage from fitting. The identity $a(h)$ is exact only under the registered count-scored rule; under the proper score the decomposition is first-order, and the measured higher-order term (0.028 nats per positive for hybrid-versus-cascade) is why the surviving edge is quoted as a bracket. That the edge collapses at M$\geq$3.5 is itself consistent with a scoring geometry whose leverage is largest where the multiplicity deficit is largest; this is a property of the metric and the catalog, not an independent physical signal.

On the model side, the b-value uncertainty dominates all M6 extrapolation by a measurable margin: the b-ensemble spans a factor of 28.8 in the 30-day regional P(M$\geq$6), while perturbing the ETAS fit by its own Mc = 3.65 refit deltas moves the same number by -6.5%; the magnitude law outweighs the triggering kernel by 26–102$\times$ across horizons (parameter table and uncertainty rationale in Section S6; no curvature-based $\pm 1\sigma$ accompanies it because the fit pins at the 0.95 branching cap, an active bound). A full pipeline refit at base Mc = 3.5 is structurally blocked by the calibration design; that arm bounds the design's transportability, not the completeness question (Section S9.2), and the label-floor sweep (Section S8) is the operative completeness evidence. The ETAS fit is isotropic and pinned at the cap; the backtest cascade is limited to K = 500 simulations; and the spatial and pseudo-likelihood rejections locate a real over-smoothing of the spatial kernel that this study diagnoses but does not correct. The GNSS null bounds this channel as engineered (the continuous-GPS geometry is weak against the offshore fault), not geodetic coupling in general, and the Sındırgı sequence exposed a hard spatial-coverage limit of the model box.

Future work follows from the mechanism. Four refinements, in priority order: a spatially varying productivity K(**x**); a time-varying background μ(**x**, t); an ML stage that predicts these ETAS parameter fields rather than the rate directly, so learned flexibility is spent inside the physics; and a spatially varying b(**x**, t) (Nandan et al., 2017), whose physical case is that the spatial variation is already measured rather than hypothesized (the local b-positive field is a per-cell input). The catalog's era- and threshold-dependence is *not* part of that case, being the conversion mixture and the rate error (Section S10.3), and the b(**x**, t) refinement is conditional on magnitude homogenization being resolved first, since on this catalog a varying b would fit the conversion mixture before it fit the crust. On the scoring side, the fix is a jointly-elicited count–occupancy pair, each axis scored on its matched functional (Brehmer et al., 2024). On the data side, a dense, machine-learning-repicked micro-catalog remains the highest-value addition (our AFAD attempt failed the promotion gate through completeness non-stationarity, pointing to per-year-completeness-normalized features on a longer validation window), with time-variable GNSS coupling on an offshore-sensitive geometry and repeating-earthquake creep observables both currently availability-limited. Finally, the hashed prospective log should be allowed to accumulate: only an out-of-sample record can establish whether the spatial discrimination shown here translates into operational value.

Supplementary material

The supplementary file contains Table S1 (principal Coulomb stress sources), Table S2 (the 19 causal features), Table S3 (catalog summary), Table S4 (the calibration battery), Table S5 (quarter- and year-ahead regional probabilities), Table S6 (the b_op count-calibration sweep), Table S7 (the recalibration challengers), Table S8 (the pre-registered run ledger), Table S9 (the machine-learning configuration), Table S10 (the foreshock false-alarm accounting), Table S11 (the ETAS parameter table), Table S12 (the label-floor sweep), Tables S13–S15 (the post-review configuration sensitivities), Tables S16–S17 (the operational-b sweep variants and extended arms), Tables S18–S22 (the post-review magnitude-law, foreshock-episode, leave-Kumburgaz-out and multiplicity analyses), Tables S23–S24 (the feature ablation and grouped principal components), and Tables S25–S27 (the operational-b verdict grid, raw occupancy totals, and findings by evidentiary tier); Figures S1–S5 (background-rate fields; the pre-event forecast map and information-arrival countdown for the 2025 Mw 6.2; discriminator reliability; the live $M \geq 3.5$ forecast map); and Sections S1–S17: the branching-ratio-preserving productivity rescale (S1), the count-scoring identity derivation (S2), the pre-registered run ledger (S3), the machine-learning configuration (S4), the foreshock false-alarm denominator (S5), the ETAS parameter table (S6), the release changelog (S7), label-floor robustness (S8), post-review configuration sensitivities (S9), the operational-b forensics (S10), the post-review analyses under a dated, hashed amendment (S11), the feature-ablation and grouped-PCA study (S12), the full information-arrival analysis of the 2025 events (S13), the conditional large-event discriminator and alert/renewal layers (S14), the calibration battery and live products (S15), engineered-channel construction details (S16), and additional verdict and summary tables

(S17).

Data and code availability

All code, processed data products, configuration files, and results artifacts are archived on Zenodo at https://doi.org/10.5281/zenodo.21535368 (Alhan & Khabat, 2026) and developed at https://github.com/keremalhan/marmara-forecast. The archive carries three machine-readable claims files: `claims.json` (the registered count-scored file that adjudicates every model comparison of record), `claims_bernoulli.json` (the secondary binary-occurrence proper-score file), and `claims_sensitivities.json` (the post-review configuration and extended-b sensitivities, exploratory by designation), together with the block-bootstrap intervals (`bootstrap_ci.json`) from which every interval in this paper is drawn. It further includes the dated, hashed pre-registration and its amendment chain, tabulated line by line in Section S3 (Table S8); the `reproduce-all` target that asserts every reported number; the placebo-battery outputs; and the pyCSEP inputs and results. Release semantics are versioned (current release 1.2.0), with an itemized changelog in Section S7; the release history changes no model and no datum relative to what is evaluated here, and the operational b_op is retained as a convention with its forensics in Section S10. The append-only, hash-stamped prospective forecast log continues to accumulate beyond the archived snapshot. The processed catalog is redistributed as a derived dataset with attribution to the Boğaziçi University Kandilli Observatory and Earthquake Research Institute Regional Earthquake-Tsunami Monitoring Center (KOERI-RETMC). GNSS velocity inputs are from the Nevada Geodetic Laboratory, and fault geometry inputs are from the GEM Global Active Faults Database. Full data-use and software license information is provided in the archived repository.

Author contributions

Basri Kerem Alhan: Conceptualization, Methodology, Data curation, Writing – original draft.
Kenessary Khabat: Software, Formal analysis, Writing – review & editing.

Competing interests

The authors declare no competing interests.

Acknowledgements

We thank the Boğaziçi University Kandilli Observatory and Earthquake Research Institute Regional Earthquake-Tsunami Monitoring Center (KOERI-RETMC) for the earthquake bulletin that underlies the catalog, the Nevada Geodetic Laboratory for the GNSS velocity solutions, and the GEM Global Active Faults Database for the fault model. This research received no external funding.

References

Aki, K. (1965). Maximum likelihood estimate of b in the formula $\log N = a - bM$ and its confidence limits. *Bulletin of the Earthquake Research Institute, 43*, 237–239.

Alhan, B. K., & Khabat, K. (2026). *Code and data for: Leakage-audited machine learning versus ETAS for earthquake forecasting in the Sea of Marmara* (Version 1.2.0) [Software]. Zenodo. https://doi.org/10.5281/zenodo.21535368

Ambraseys, N. (2002). The seismic activity of the Marmara Sea region over the last 2000 years. *Bulletin of the Seismological Society of America, 92*(1), 1–18. https://doi.org/10.1785/0120000843

Bayona, J. A., Savran, W. H., Rhoades, D. A., & Werner, M. J. (2022). Prospective evaluation of multiplicative hybrid earthquake forecasting models in California. *Geophysical Journal International, 229*(3), 1736–1753. https://doi.org/10.1093/gji/ggac018

Blewitt, G., Hammond, W. C., & Kreemer, C. (2018). Harnessing the GPS data explosion for interdisciplinary science. *Eos, 99*. https://doi.org/10.1029/2018EO104623

Brehmer, J. R., Gneiting, T., Herrmann, M., Marzocchi, W., Schlather, M., & Strokorb, K. (2024). Comparative evaluation of point process forecasts. *Annals of the Institute of Statistical Mathematics, 76*(1), 47–71. https://doi.org/10.1007/s10463-023-00875-5

Dascher-Cousineau, K., Shchur, O., Brodsky, E. E., & Günnemann, S. (2023). Using deep learning for flexible and scalable earthquake forecasting. *Geophysical Research Letters, 50*(17), e2023GL103909. https://doi.org/10.1029/2023GL103909

Ertuncay, D., Büyükakpınar, P., Fornasari, S. F., & Tan, O. (2025). 23 April 2025 Marmara Sea (Mw 6.3), Türkiye earthquake: Mainshock, aftershock, and ground observations. *Seismica, 4*(2), 1773. https://doi.org/10.26443/seismica.v4i2.1773

Ferro, C. A. T. (2014). Fair scores for ensemble forecasts. *Quarterly Journal of the Royal Meteorological Society, 140*(683), 1917–1923. https://doi.org/10.1002/qj.2270

Geller, R. J., Jackson, D. D., Kagan, Y. Y., & Mulargia, F. (1997). Earthquakes cannot be predicted. *Science, 275*(5306), 1616. https://doi.org/10.1126/science.275.5306.1616

Gulia, L., & Wiemer, S. (2019). Real-time discrimination of earthquake foreshocks and aftershocks. *Nature, 574*(7777), 193–199. https://doi.org/10.1038/s41586-019-1606-4

Hainzl, S., Kumazawa, T., & Ogata, Y. (2024). Aftershock forecasts based on incomplete earthquake catalogues: ETASI model application to the 2023 SE Türkiye earthquake sequence. *Geophysical Journal International, 236*(3), 1609–1620. https://doi.org/10.1093/gji/ggae006

Hardebeck, J. L., Llenos, A. L., Michael, A. J., Page, M. T., Schneider, M., & van der Elst, N. J. (2024). Aftershock forecasting. *Annual Review of Earth and Planetary Sciences, 52*, 61–84. https://doi.org/10.1146/annurev-earth-040522-102129

Helmstetter, A., Kagan, Y. Y., & Jackson, D. D. (2006). Comparison of short-term and time-independent earthquake forecast models for southern California. *Bulletin of the Seismological Society of America, 96*(1), 90–106. https://doi.org/10.1785/0120050067

Jordan, T. H., Chen, Y.-T., Gasparini, P., Madariaga, R., Main, I., Marzocchi, W., Papadopoulos, G., Sobolev, G., Yamaoka, K., & Zschau, J. (2011). Operational earthquake forecasting: State of knowledge and guidelines for utilization. *Annals of Geophysics, 54*(4), 315–391. https://doi.org/10.4401/ag-5350

Jover-Alfaro, J., Arias-Antúnez, E., & Mateo-Cortés, J. (2026). Forecasting earthquakes by Machine Learning techniques: lights and shadows. *Earth Science Informatics, 19*, 24.

https://doi.org/10.1007/s12145-026-02078-x

Kadirioğlu, F. T., & Kartal, R. F. (2016). The new empirical magnitude conversion relations using an improved earthquake catalogue for Turkey and its near vicinity (1900–2012). *Turkish Journal of Earth Sciences, 25*(4), 300–310. https://doi.org/10.3906/yer-1511-7

Kagan, Y. Y. (2010). Statistical distributions of earthquake numbers: Consequence of branching process. *Geophysical Journal International, 180*(3), 1313–1328. https://doi.org/10.1111/j.1365-246X.2009.04487.x

Kagan, Y. Y., & Jackson, D. D. (2000). Probabilistic forecasting of earthquakes. *Geophysical Journal International, 143*(2), 438–453. https://doi.org/10.1046/j.1365-246X.2000.01267.x

Kapoor, S., & Narayanan, A. (2023). Leakage and the reproducibility crisis in machine-learning-based science. *Patterns, 4*(9), 100804. https://doi.org/10.1016/j.patter.2023.100804

King, G. C. P., Stein, R. S., & Lin, J. (1994). Static stress changes and the triggering of earthquakes. *Bulletin of the Seismological Society of America, 84*(3), 935–953. https://doi.org/10.1785/BSSA0840030935

Martínez-Garzón, P., Chen, X., Becker, D., Núñez-Jara, S., Kartal, R. F., Türker, E., Dresen, G., Ben-Zion, Y., Jara, J., Cotton, F., Kadirioğlu, F. T., Kılıç, T., & Bohnhoff, M. (2026). Progressive eastward rupture of the Main Marmara Fault toward Istanbul. *Science, 391*(6783), 379–383. https://doi.org/10.1126/science.adz0072

Mizrahi, L., Nandan, S., & Wiemer, S. (2021). The effect of declustering on the size distribution of mainshocks. *Seismological Research Letters, 92*(4), 2333–2342. https://doi.org/10.1785/0220200231

Mizrahi, L., Dallo, I., van der Elst, N. J., Christophersen, A., Spassiani, I., Werner, M. J., Iturrieta, P., Bayona, J. A., Iervolino, I., Schneider, M., Page, M. T., Zhuang, J., Herrmann, M., Michael, A. J., Falcone, G., Marzocchi, W., Rhoades, D., Gerstenberger, M., Gulia, L., Schorlemmer, D., Becker, J., Han, M., Kuratle, L., Marti, M., & Wiemer, S. (2024). Developing, testing, and communicating earthquake forecasts: Current practices and future directions. *Reviews of Geophysics, 62*(3), e2023RG000823. https://doi.org/10.1029/2023RG000823

Nandan, S., Ouillon, G., Wiemer, S., & Sornette, D. (2017). Objective estimation of spatially variable parameters of epidemic type aftershock sequence model: Application to California. *Journal of Geophysical Research: Solid Earth, 122*(7), 5118–5143. https://doi.org/10.1002/2016JB013266

Ogata, Y. (1988). Statistical models for earthquake occurrences and residual analysis for point processes. *Journal of the American Statistical Association, 83*(401), 9–27. https://doi.org/10.1080/01621459.1988.10478560

Okada, Y. (1992). Internal deformation due to shear and tensile faults in a half-space. *Bulletin of the Seismological Society of America, 82*(2), 1018–1040. https://doi.org/10.1785/BSSA0820021018

Parsons, T. (2004). Recalculated probability of M $\geq$ 7 earthquakes beneath the Sea of Marmara, Turkey. *Journal of Geophysical Research: Solid Earth, 109*(B5), B05304. https://doi.org/10.1029/2003JB002667

Politis, D. N., & Romano, J. P. (1994). The stationary bootstrap. *Journal of the American Statistical Association, 89*(428), 1303–1313. https://doi.org/10.1080/01621459.1994.10476870

Rhoades, D. A., Schorlemmer, D., Gerstenberger, M. C., Christophersen, A., Zechar, J. D., & Imoto, M. (2011). Efficient testing of earthquake forecasting models. *Acta Geophysica, 59*(4), 728–747. https://doi.org/10.2478/s11600-011-0013-5

Savran, W. H., Werner, M. J., Marzocchi, W., Rhoades, D. A., Jackson, D. D., Milner, K., Field, E., & Michael, A. (2020). Pseudoprospective evaluation of UCERF3-ETAS forecasts during the 2019 Ridgecrest sequence. *Bulletin of the Seismological Society of America, 110*(4), 1799–1817. https://doi.org/10.1785/0120200026

Savran, W. H., Bayona, J. A., Iturrieta, P., Asim, K. M., Bao, H., Bayliss, K., Herrmann, M., Schorlemmer, D., Maechling, P. J., & Werner, M. J. (2022). pyCSEP: A Python toolkit for earthquake forecast developers. *Seismological Research Letters, 93*(5), 2858–2870. https://doi.org/10.1785/0220220033

Serafini, F., Naylor, M., Lindgren, F., Werner, M. J., & Main, I. (2022). Ranking earthquake forecasts using proper scoring rules: Binary events in a low probability environment. *Geophysical Journal International, 230*(2), 1419–1440. https://doi.org/10.1093/gji/ggac124

Stockman, S., Lawson, D. J., & Werner, M. J. (2026). EarthquakeNPP: A benchmark for earthquake forecasting with neural point processes. *Transactions on Machine Learning Research.* https://openreview.net/forum?id=dIcNAg6ZuZ

Styron, R., & Pagani, M. (2020). The GEM Global Active Faults Database. *Earthquake Spectra, 36*(S1), 160–180. https://doi.org/10.1177/8755293020944182

van der Elst, N. J. (2021). B-positive: A robust estimator of aftershock magnitude distribution in transiently incomplete catalogs. *Journal of Geophysical Research: Solid Earth, 126*(2), e2020JB021027. https://doi.org/10.1029/2020JB021027

Veen, A., & Schoenberg, F. P. (2008). Estimation of space–time branching process models in seismology using an EM-type algorithm. *Journal of the American Statistical Association, 103*(482), 614–624. https://doi.org/10.1198/016214508000000148

Vere-Jones, D. (1998). Probabilities and information gain for earthquake forecasting. *Computational Seismology, 30*, 248–263.

Werner, M. J., Zechar, J. D., Marzocchi, W., & Wiemer, S. (2010). Retrospective evaluation of the five-year and ten-year CSEP-Italy earthquake forecasts. *Annals of Geophysics, 53*(3), 11–30. https://doi.org/10.4401/ag-4840

Wiemer, S., & Wyss, M. (2000). Minimum magnitude of completeness in earthquake catalogs: Examples from Alaska, the western United States, and Japan. *Bulletin of the Seismological Society of America, 90*(4), 859–869. https://doi.org/10.1785/0119990114

Yavas, C. E., Chen, L., Kadlec, C., & Ji, Y. (2024). Improving earthquake prediction accuracy in Los Angeles with machine learning. *Scientific Reports, 14*, 24440. https://doi.org/10.1038/s41598-024-76483-x (Retraction published 2026, https://doi.org/10.1038/s41598-026-49689-4)

Zechar, J. D., & Jordan, T. H. (2008). Testing alarm-based earthquake predictions. *Geophysical Journal International, 172*(2), 715–724. https://doi.org/10.1111/j.1365-246X.2007.03676.x

Zechar, J. D., & Zhuang, J. (2014). A parimutuel gambling perspective to compare probabilistic seismicity forecasts. *Geophysical Journal International, 199*(1), 60–68. https://doi.org/10.1093/gji/ggu137

Zhuang, J., Ogata, Y., & Vere-Jones, D. (2002). Stochastic declustering of space–time earthquake occurrences. *Journal of the American Statistical Association, 97*(458), 369–380. https://doi.org/10.1198/016214502760046925